UNCLASSIFIED

Defense Technical Information Center Compilation Part Notice

ADP011141

TITLE: Design and Testing of a Mesoscale Actuator Device

DISTRIBUTION: Approved for public release, distribution unlimited

This paper is part of the following report:

TITLE: Active Control Technology for Enhanced Performance Operational Capabilities of Military Aircraft, Land Vehicles and Sea Vehicles [Technologies des systemes a commandes actives pour l'amelioration des performances operationnelles des aeronefs militaires, des vehicules terrestres et des vehicules maritimes]

To order the complete compilation report, use: ADA395700

The component part is provided here to allow users access to individually authored sections of proceedings, annals, symposia, etc. However, the component should be considered within the context of the overall compilation report and not as a stand-alone technical report.

The following component part numbers comprise the compilation report:
ADP011101 thru ADP011178

UNCLASSIFIED

DESIGN AND TESTING OF A MESOSCALE ACTUATOR DEVICE

Joon Park, Scott Keller, Gregory P. Carman, and H. Thomas Hahn

Mechanical and Aerospace Engineering Department
University of California, Los Angeles
48-121 Eng. IV, Los Angeles, CA 90095-1597, USA

ABSTRACT

Design and testing of a mesoscale actuator device is presented in this paper. The device uses frequency rectification concepts to amplify the displacements while retaining comparable force outputs to current piezoelectric actuators. The design is based on an inchworm motor with the exception that microridges are used in the clamping system. A FEM model is used to design a device that produces a peak to peak amplitude of 900N at 11 mm/sec with a weight of 100 g (i.e. specific power of 99 W/kg). A prototype device is fabricated and tested with excellent agreement between analysis and testing results. Stress and modal analysis are used to demonstrate that the device has an infinite fatigue life and a first modal frequency at 1777 Hz.

Keywords: frequency rectification, inchworm motor, piezoelectric stack, microridges

INTRODUCTION

Active materials are being used in a wide range of applications including vibration reduction [1-6], noise suppression [7], adaptive optics [8-10], and solid-state motors [11-16]. For example, vibration in rotorcraft is a major problem resulting in fatigue, poor ride quality, high noise levels, deficiencies in handling qualities, and reduction of weapons system effectiveness [1-4]. One of the promising methods for reducing rotorcraft vibration is an Actively Controlled Flap (ACF) [3]. By articulating the flap ± 3° the vibration can theoretically be decreased by 90%. While AFC concepts are promising, developing an actuator system to produce sufficient flap deflection represents a major obstacle.

One approach to overcome the displacement limitation is to use frequency rectification concepts. Frequency rectification ideally increases displacements while retaining high force output. This is in sharp contract to displacement amplification techniques that increase displacements by reducing force output. Mender-line actuators [17-19] are an example of displacement amplification techniques while inchworm motors [11-12,14,16,20-22] and ultrasonic motors [13] are examples of frequency rectification concepts. Among these actuators, the inchworm motor is a popular device due to its large travel distance (mm) and precise positioning capability (submicron). While producing large displacements, current frequency rectification devices have limited force outputs.

Burleigh Instruments Inc. introduced the first inchworm linear motor mechanism in 1975. This inchworm provides nanometer resolution, a linear travel range of 200 mm, a speed of 2 mm/sec, and an output force of 1.5 kgf [20]. Recent research has focused on increasing the force and velocity output of these linear motors. For example, a hybrid transducer-type linear motor was developed for high speed [21]. The motor produced velocities of 50 cm/sec, but the force output was limited to 0.5 kgf. Miesner and Teter [22] designed a linear motor to produce large force output using piezoelectric stacks for clamping and a magnetostrictive material TERFENOL-D for stepping. The relatively large prototype (200 mm x 200 mm x 20 mm) is reported to provide a stall load of 10 kgf and a no-load speed of 2.54 cm/sec. Zhang and Zhu developed a linear motor using a monolithic flexure frame and a guideway to transfer large mechanical loads [12]. Although analysis showed that it could produce a 20 kgf force output, a large clamping region of 25 mm x 25 mm was required. Based on these reviews, the principal limitation of the linear motors are the force outputs and their relative size.

The clamping system in the linear motor determines the force output. Most linear motors use static friction as the clamping mechanism. This is limited by the coefficient of friction which is usually 0.2 ~ 0.3. Increasing the coefficient of friction by roughening the surfaces and applying a clamping preload improves load transfer, but causes other problems associated with positioning, disengaging, and wear [12, 22]. Electrostatic clamping [15] and electrorheological (ER) clamping [23] have also been attempted, but the clamping forces produced were less than 1 kgf. Recently mechanical locking MEMS ridges were used in a Mesoscale Actuator Device (similar to an inchworm motor) to replace the frictional clamp [24]. The feasibility of the MEMS ridges was tested and validated for interlocking efficiency, load transfer capability (36 MPa), and engagement frequency up to 500 Hz [25-27]. However, a detailed design of an operational frequency rectification device was not presented.

The main objective of this study is to design a device that integrates piezoelectric stacks and MEMS ridges in a linear motor design. FEM analysis is used to design a prototype device that is subsequently tested. The device is designed to push and pull 450N (i.e. peak to peak amplitude of 900N) at 11 mm/sec in a relative compact size (72 mm x 32 mm x 6.5 mm). The specific power for the device is calculated to be 99 W/kg neglecting the mass associated with power supplies.

DESIGN OF MESOSCALE ACTUATOR DEVICE

An illustration of the device is shown in Fig. 1. It contains four sets of MEMS ridges, three piezoelectric stacks, two guide rods, and a housing. The housing includes ridge blocks for

Paper presented at the RTO AVT Symposium on "Active Control Technology for Enhanced Performance Operational Capabilities of Military Aircraft, Land Vehicles and Sea Vehicles", held in Braunschweig, Germany, 8-11 May 2000, and published in RTO MP-051.

attachment of the MEMS ridges and load blocks to transfer mechanical loads from the housing to the piezoelectric stack. The housing is attached to a structure through bolts in the middle of the casing. The middle casing is also adhered to the structure to further enhance load transfer. The three critical features that determine power output of the device are the piezoelectric stacks, MEMS ridges, and housing.

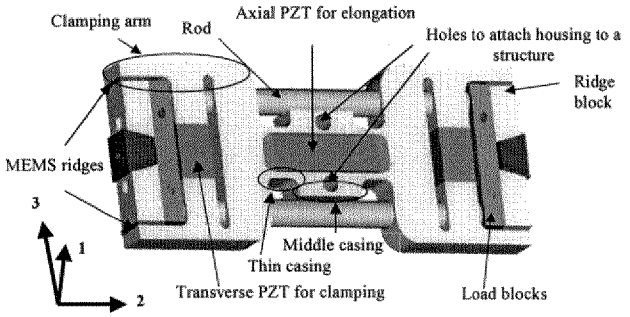

Fig. 1 A prototype device

There are several beneficial features associated with the piezoelectric design in the device. First, without an applied voltage (i.e. fail safe), all four ridges are engaged and the device is locked into place. Another advantage associated with the design is that only positive electric field are applied to disengage and engage as well as to elongate or contract the inchworm motor. This reduces hysteresis, eliminates ferroelectric switching, and reduces fatigue degradation. In addition, the axial piezoelectric stack is preloaded with a 450N compression load. This mechanical bias allows the piezoelectric stack to externally pull 450N in addition to pushing 450N (stack takes up to 1000N). All of the piezoelectric stacks experience only compressive loads, i.e. absence of shear and tension loads.

Stack selection is based on electrical and mechanical properties including capacitance, resonant frequency, piezoelectric constants, and Young's modulus. In general, a low capacitance is preferred for high-speed operation since the required current is proportional to capacitance. The system is designed for a low voltage amplifier. For the characterization of piezoelectric stacks in the device, the reader is referred to reference [28].

A trapezoidal MEMS ridge is used in the clamping system of the device (see Fig. 2). The trapezoidal microridges offer substantial improvement over rectangular microridges by providing easy engagement and high shear strength [26]. These ridges are fabricated out of single crystal silicon and have a shear strength of 36 MPa. Two critical dimensions of the ridges are its height and pitch. The height (5 μm) of the ridges represents a minimum displacement that must be produced by the transverse (clamping) piezoelectric stack. One pitch (11 μm) of the ridge represents a minimum step that must be produced by elongation of the axial piezoelectric stack. For a detailed discussion on the MEMS ridge fabrication process, the reader is referred to references [25-27].

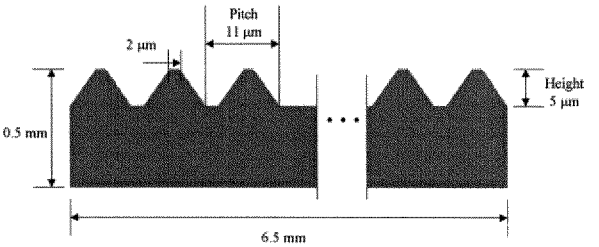

(a) Schematic diagram of trapezoidal microridges

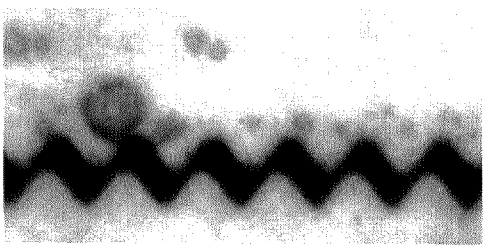

(b) SEM picture of microridges

Fig. 2 Microridges used in the device

Another important consideration is the housing design. The housing design and material significantly influences the weight of the device and impacts the specific power. In addition to weight, the housing must be sufficiently stiff to prevent excessive deformation. Materials such as aluminum, titanium, and steel were considered, but steel was chosen because of its high stiffness. For a detailed discussion on the results obtained with other materials, the reader is referred to reference [27].

One complete cycle of operation consists of seven steps. These steps produce an axial displacement of 11 μm (one pitch of the ridge). Operating the device at 1 kHz produces a nominal speed of 11 mm/sec (11 μm x 1000 sec^{-1}). The operation sequence of the device is shown in Fig. 3.

(a) All ridges are engaged and locked at 0 volt.
(b) Right ridges are disengaged by elongation of the right transverse piezoelectric.
(c) Elongation of the axial piezoelectric moves the rods to the left relative to the housing.
(d) Right ridges are engaged again.
(e) Left ridges are disengaged by elongation of the left transverse piezoelectric.
(f) Contraction of the axial piezoelectric moves the rods to the left relative to the housing.
(g) Left ridges are engaged to complete the cycle.

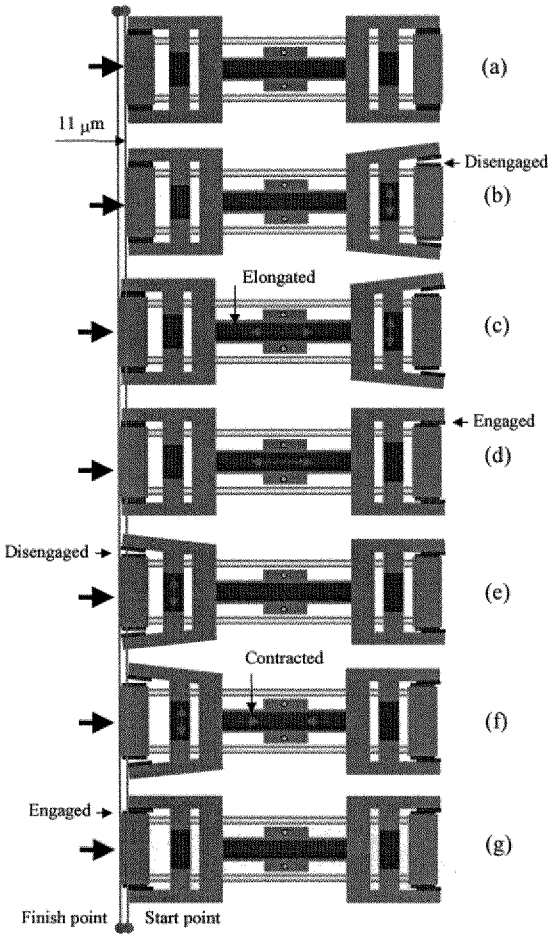

Fig. 3 Operation sequence of the device

A preliminary analysis of the device using a simple 1-D piezoelectric model coupled with a uniform beam analysis was performed. Specifically, two areas of the housing, the thin casing and the clamping arm (see Fig. 1), were initially sized. The thin casing should permit an axial displacement of 11 μm (i.e. pitch of ridge) under mechanical loads (i.e. 450N external load plus a 450N internal mechanical bias load) while the clamping arm should permit a 5-μm (i.e. height of ridge) displacement at the ridges. In the preliminary analysis, a maximum electric field of 3 MV/m (~350 volts) was permitted but this large value was not required in the actual design. These requirements produced an initial design to begin a more detailed analysis.

A more detailed analysis using a coupled finite element model is required to adequately design the system. This model is based on the preliminary results obtained from the simple analysis. ANSYS version 5.5 was used because it provides a coupled-field analysis [29]. Several assumptions were made in developing the FEM analysis. First, it is assumed the problem is plane stress ($\sigma_{11} = \sigma_{12} = \sigma_{13} = 0$). This is reasonable because the device is load free and thin in the 1 direction. In the local coordinate system, the 1 direction is the thickness direction of the device while the 2 direction is the polarization direction of the axial piezoelectric stack (see Fig. 1). Second, the piezoelectric is assumed to be linear. Third, temperature is constant at room temperature. Fourth, steel and silicon are isotropic while the piezoelectric is transversely isotropic. Finally, the piezoelectric stacks can be modeled as a monolithic piezoelectric. The constitutive coupled equations for a piezoelectric are

$$\begin{aligned} \sigma_{ij} &= c^{E}_{ijkl}\varepsilon_{kl} - g_{mij}E_m \\ D_m &= g_{mij}\varepsilon_{ij} + e^{\varepsilon}_{mp}E_p \end{aligned} \tag{1}$$

where σ_{ij} is stress, c^{E}_{ijkl} is stiffness at constant electric field, ε_{ij} is strain, g_{mij} is piezoelectric coupling coefficients, E_m is electric field, D_m is electric displacement, and e^{ε}_{mp} is dielectric permittivity at constant strain. The piezoelectric coupling coefficients, g_{mij}, can be obtained by taking an inner product ($g_{mkl} = c^{E}_{ijkl}\, d_{mij}$). The general relationship between the displacement and the voltage are

$$\begin{aligned} \varepsilon_{ij} &= \frac{1}{2}(u_{i,j} + u_{j,i}) \\ E_i &= -\phi_{,i} \end{aligned} \tag{2}$$

where u_i is displacement and ϕ is electric potential (voltage). ANSYS uses linear interpolation functions to approximate the displacements and voltages. These relations are used to satisfy the governing equations in the average sense. The governing equations are

$$\begin{aligned} \sigma_{ij,i} &= \rho\ddot{u}_j \\ D_{i,i} &= q \end{aligned} \tag{3}$$

where ρ is the density and q is charge. The dot above the displacement of u signifies partial time differentiation. By substituting Eq. (2) into (1) and subsequently into (3), a numerical method can be used to solve for the static and dynamic response of a structural analysis. Solution to these equations can be used to predict stresses, displacements, and mode shapes.

Two element types were used in the model. One element type is a 2-D plane stress solid structure for steel and silicon. The other element type is a 2-D element for piezoelectric materials that has structural field capability with limited coupling between the fields. The total number of elements used in the mesh is 3844. Those areas expected to have high stress concentration were meshed with a finer mesh compared to other areas. Mesh refinement techniques were used to verify that the stress values had converged. Static analysis was used to evaluate stresses and displacements while modal analysis was used to predict the resonance frequencies.

The housing is physically attached by bolt holes to a rigid structure (see Fig. 1). Therefore, the displacement boundary condition at/near the bolt holes is fixed and can be best represented by 0 displacement in the x and y direction. A reaction load defined by F_R is used to represent the load on the housing due to the mechanical preload (450N) on the stack. In addition to the reaction load, an external mechanical load is also applied to the device. The external load can vary from a maximum compressive load of 450N to a maximum tensional load of 450N. A wide range of external mechanical loads were studied [30] with the worst case scenarios presented in this paper. The worst loading case scenario is a maximum compressive load of 900N on the stack (i.e. external

compression mechanical load of 450N plus preload of 450N). The voltage on the piezoelectric stack is applied as a potential difference ($\Delta\phi$) between the two ends of the piezoelectric rather than each individual layer. This is acceptable if the global response of the piezoelectric stack is desired rather than internal stress/elastic field concentration in the stack.

Based on stresses obtained in the static results, a fatigue analysis was used to determine the life of the device. The endurance limit and tensile strength for the steel used in the housing (steel 4340) is 381 MPa and 774 MPa, respectively [31]. The modified endurance limit for fatigue was calculated using the equation by Marin [32]. The safety factor was found using the modified Goodman relation.

PROTOTYPE FABRICATION AND TESTING

A prototype device (see Fig. 4) was fabricated using a CNC milling machine. The prototype was used to evaluate translation and clamping mechanisms at low frequencies without an external load. Aluminum was used for the prototype device. Generally, aluminum is easier to machine than steel. The fabrication of a steel structure requires Electrical Discharge Machining (EDM) technique which was not available at the time when these tests were conducted.

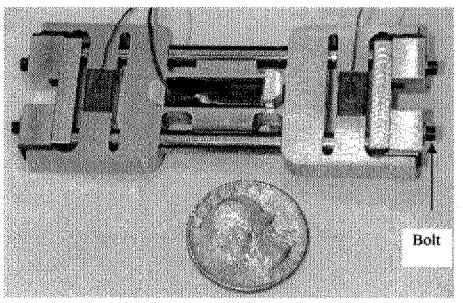

Fig. 4 Prototype device

Assembling the device is a critical process. There are several steps in assembling the device. Integrating the guide rods into the housing is a first step. This is done by honing the guide holes in the housing until an acceptable fit is obtained. If the fit is too loose, the microridges will become unaligned after a few stepping sequences. The second step is to integrate the axial piezoelectric stack in the housing. The position of the stack is adjusted and preloaded with a spacer until symmetrical displacements are produced. The spacer has a set screw that can be turned to preload the stacks up to 450N with an internal mechanical bias. Third, the transverse piezoelectric stacks are inserted. The mechanical slots are mechanically stretched until they are sufficiently wide to accommodate the stack. The return force from this distortion is sufficient to marginally preload the stacks and mechanically retain them during operation.

Mounting the ridges is the last step. The ridges are mounted in several stages. There are a total of eight ridges. Four ridges are first mounted to ridge blocks (one ridge for one ridge block) using TRA-BOND F113 epoxy adhesive. Each of four ridges is then engaged with one of the other four ridges. Each set (4 sets) of ridges is kept engaged until their introduction to the device. The assembled ridge blocks with the engaged ridges are mounted on the clamping arm using an epoxy adhesive. The assembled ridge blocks are then assembled to the load blocks with bolts (See Fig. 1 & Fig. 4). Assembly in this manner ensures proper spacing and engagement of the ridges on an assembled device.

Adhesives used to adhere the microridges to the device was evaluated. Two different epoxy adhesives were studied. One is fast cure epoxy adhesive, Araldite 2043 90-second multi-purpose epoxy adhesive, and the other is slow cure epoxy adhesive, TRA-BOND F113 high impact optically clear epoxy adhesive. These two epoxy adhesive are easy to handle, available, and low cost. Pot life and cure time are 90 seconds and 2 hours for the fast cure adhesive and 2 hours and 24 hours for the slow cure adhesive.

The bonding strength for steel-to-silicon was measured based on a single lap shear test (ASTM D1002) with some modifications. The modification was necessary since silicon cannot be gripped in a testing machine. Two steel pieces (air-hardened precision ground flat stock, AISI-SAE D-2) were adhered to a diced silicon wafer. The steel was prepared based on ASTM standard dimensions (101.6 mm x 25 mm and 1.62 mm). The silicon was prepared from one-side polished (100) wafers with thickness of 0.5 mm. The overlapped area was 12.7 mm x 25 mm based on the ASTM D1002. To minimize any bending and distortion caused by unaligned loading due to thickness of specimen, two extra steel plates were inserted into the grips. The specimens were loaded at a rate of 0.26 mm/min. Seven specimens for each adhesive were tested.

The prototype device was tested in a probe station. The piezoelectric stacks in the device were driven with a TREK model 50/750 High Voltage (HV) power supply. Dial gauge (see Fig. 5) was used to measure the travel distance of the device. Before operation, various voltages were manually applied to find the voltages required to produce an axial 11-μm displacement and a transverse 5-μm displacement. The required voltages were entered into the control software to operate the device 11, 110, 550, and 880 μm back and forth in the frequency range of 1 to 80 Hz. The testing was limited to 80 Hz due to limitations of the amplifier (100 mA) at 250 volts. The amplifier cannot supply the required current to operate the piezoelectric stack dynamically at frequencies larger than 80 Hz if the applied voltage is higher than 250 volts. A 1 kHz frequency is possible with a higher current amplifier.

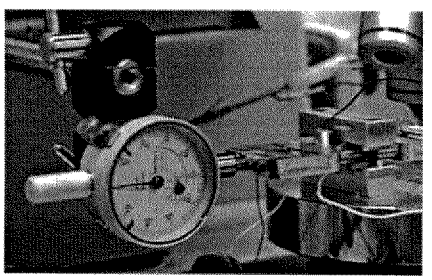

Fig. 5 Testing setup

RESULTS AND DISCUSSION

The FEM analysis was used to predict displacements and stresses in the device. The static analysis was first used to evaluate the axial displacements of the ridges due to elongation of the axial piezoelectric stack. An external mechanical load of

450N (compression) as well as an internal reaction load of 450N was applied in the model. Therefore, the maximum compression load on the piezoelectric is 900N load ($F_E + F_R$). This represents a worst case loading scenario. The axial displacement between the left and the right ridges is larger than 11 μm when a 330 volts is applied on the axial stack. This displacement is calculated by adding the displacement of 2.71 μm at left ridges and the displacement of 8.77 μm at the right ridges. This result indicates that the device can step the necessary 11 μm under a maximum compression load.

Similarly, a transverse displacement due to elongation of the transverse piezoelectric using static analysis is evaluated. Since the transverse piezoelectric stack is loaded only with a moderate compressive loading, a reaction load due to the small preload is not required. The displacement at ridges indicates that a 5.13-μm displacement is produced when 257 volts is applied to the transverse piezoelectric stack. This result verifies that the ridges can be engaged and disengaged in the device.

To evaluate the accuracy of the FEM model, the data was compared to experimental results. The required voltages for the transverse piezoelectric stack and the axial piezoelectric stack in the aluminum prototype without a external mechanical load were measured to be 225 volts and 235 volts, respectively. The displacements were measured using a microscope with a resolution of ± 0.25 μm. When the experimental results are compared to FEM results, the discrepancy is less than 6.7%. The result confirms that the finite element analysis is accurate and sufficient to predict actual static motion of the device.

The static analysis results were also used to assess the device durability. A fatigue analysis based on Von Mises stresses was used. The "worst" case scenario of maximum voltage and maximum mechanical load was used to evaluate fatigue life. These conditions are voltage (330 volts) and tension or compressive mechanical loads of 900N ($F_E + F_R$). As mentioned in the earlier section, two areas of the housing, the thin casing and the clamping arm, are potential fatigue failure regions during operation. The contour plot of Von Mises stress in the casing area of the housing (see Fig. 1) is shown Fig. 6(a). At the casing, the maximum and minimum Von Mises stress during operation is found to be 381 MPa and 0.8 MPa, respectively. Based on these stresses, the safety factor for fatigue is 1.17 using the modified Goodman relation. Safety factors higher than 1 indicate fatigue failure in this area does not likely occur during operation. Another possible fatigue failure region occurs at the end of the clamping arm, in Fig. 6(b), as shown in the contour plot of Von Mises stress. The maximum and minimum stress is 64.3 MPa and 0 MPa, respectively. The safety factor for the fatigue is calculated to be 5.76. Therefore, based on these results, the device can continuously operate for infinite life ($>10^8$) without fatigue failure.

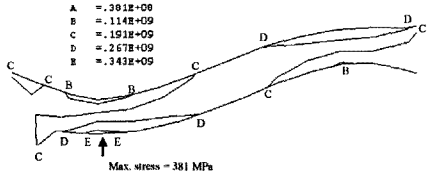

(a) Contour plot of Von Mises stress at the casing in the device

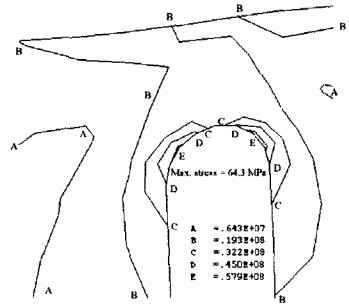

(b) Contour plot of Von Mises stress at the end of clamping arm

Fig. 6 Contour plots of Von Mises stress created using FEM

Resonance frequencies of the unloaded device as well as mode shapes were found using modal analysis. The first mode shape of the device is a bending mode. The first resonance frequency is 1777 Hz which is higher than the operational frequency of the device at 1 kHz. The next two natural frequencies occur at 1817 Hz and 5487 Hz, respectively. When mechanical loaded or small amounts of damping is added, the frequencies should be further shifted upward. These results indicate that the device can be operated at 1 kHz.

The bonding strength of adhesives used to mount the ridges was measured. Based on the single lap shear test, the bonding strength of the fast cure epoxy was much lower than the bonding strength of slow cure epoxy. The average bonding strength of the fast cure and slow cure adhesive is 2.68 MPa and 7.22 MPa with a standard deviation of 0.47 MPa and 3.31 MPa, respectively. Most specimens had failures of the adhesive at the interface between silicon and adhesive suggesting poor surface preparation. In the strength test that yielded the highest value, it was observed that a uniform adhesive layer existed with few voids. Therefore, the bonding strength tests confirm that the adhesive can support more than 450N shear load with two engaged ridge sets of 6 mm x 6.5 mm glued area.

A prototype was tested for motion at different speeds. In Fig. 7, a plot of displacements versus time for three different frequencies is illustrated. For continuous stepping of the device, a voltage of 235 volts for both the transverse and axial piezoelectric stack was used in the control software to simplify the control program. Successful forward and backward linear motion was observed at all frequencies. This linear motion of the prototype using MEMS ridges validated that MEMS ridges successfully replaced the static friction as clamping system of the linear motors with potential higher load transfer.

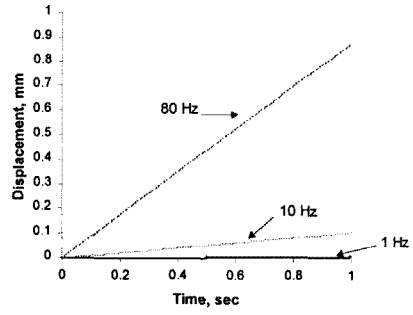

Fig. 7 Displacements measured under three different frequencies

CONCLUSIONS

A device producing large displacements and large force outputs was designed using FEM analysis. The analysis demonstrated that the device can step the necessary 11-μm displacement for the worst case loading scenario at 1 kHz. The bonding strength of the adhesives was also evaluated to ensure that failure does not occur in the bonded area of the ridges on the clamping arm. Results indicate that the adhesive supports more than 450N shear load required. An aluminum prototype device was fabricated and tested. Under open-loop control, continuous forward and backward stepping motion was observed at frequencies up to 80 Hz. Excellent agreement between the analysis and testing results was observed with a discrepancy less than 6.7 %.

ACKNOWLEDGEMENT

The authors gratefully acknowledge the support from John Prater, contract monitor, and the Army Research Office under the contract number DAAH04-95-1-0095.

REFERENCES

1. Walz, C. and I. Chopra. 1994. "Design and Testing of a Helicopter Rotor Model with Smart Trailing Edge Flaps," Presented at the 35th Structures, Structural Dynamics and Materials Conference, Adaptive Structures Forum, April 1994:309-319.
2. Narkiewicz, J. P. and G. T. S. Done. 1994. "Overview of Smart Structure Concepts for Helicopter Rotor Control," Presented at 2nd European Conf. on Smart Structures and Materials, Glasgow 1994:242-245.
3. Friedmann, P. P. and T. A. Millot. 1995. "Vibration Reduction in Rotorcraft Using Active Control: A Comparison of Various Approaches," Journal of Guidance, Control, and Dynamics, 18(4):664-673.
4. Spencer, B. T. and I. Chopra. 1996. "Design and Testing of a Helicopter Trailing Edge Flap with Piezoelectric Stack Actuator," Presented at SPIE's 1996 Symposium on Smart Structures and Materials, February 1996:120-131.
5. Tzou, H. S. 1991. "Design of a piezoelectric exciter/actuator for micro-displacement control: theory and experiment," J. J. Soc. For Prec. Eng., 13(2):104-110.
6. Tiersten, H. F. 1969. "Linear piezoelectric plate vibrations," Plenum Press, New York:55.
7. Koshigoe, S. and J. W. Murdock. 1993. "A Unified Analysis of Both Active and Passive Damping for a Plate with Piezoelectric Transducers," J. Acoust. Soc. Am. 93(1):346-355.
8. Jones, L. D., D. V. Newton, and E. Garcia. 1993. "Adaptive Devices for Precise Position Control," Proceedings of the SPIE, 1917:648-659.
9. Toshiyoshi, H., H. Fujita, T. Kawai, and T. Ueda. 1993. "Piezoelectrically operated actuators by quartz micromachining for optical application," Proceedings of IEEE Micro Electro Mechanical Systems:133-138.
10. Jones, L. and E. Garcia. 1994. "Self-sensing Control as Applied to a PZT Stack Actuator used as Micropositioner," Proceedings of the SPIE, 2190:228-237.
11. Bexell, M, A. L. Tiensuu, J. A. Schweitz, J. Soderkvist, and S. Johansson. 1994. "Characterization of an inchworm prototype motor," Sensors and Actuator A, 43: 322-329.
12. Zhang, B. and Z. Q. Zhu. 1994. "Design of an Inchworm-type Linear Piezomotor," Proceedings of the SPIE, 2190:528-539.
13. Morita, T., M. Kurosawa, and T. Higuchi. 1995. "An ultrasonic motor using bending cylindrical transducer based on PZT thin film," in Proc. of 1995 IEEE MEMS: 49-54.
14. Shimizu, N., T. Kimura, T. Nakamura, and I. Umebu. 1990. "An Ultrahigh Vacuum Scanning Tunneling Microscope with a New Inchworm Mechanism," Journal of Vac. Sci. Technol. A, 8:333-335.
15. Judy, J. W., D. L. Polla, and W. P. Robbins. 1990. "A Linear Piezoelectric Stepper Motor With Submicrometer Step Size and Centimeter Travel Range," IEEE Transactions on Ultrasonics, Ferroelectrics, and Frequency Control, 37(5):428-437.
16. Olin, H. 1994. "Design of a scanning probe microscope," J. of Measurement Science and Technology, 5: 976-984.
17. Robbins, W. P. 1995. "Ferroelectric-Based Microactuators," Integrated Ferroelectrics, 11:179-190.
18. Polla, D. L. 1997. "Application of PZT Thin Films in Microelectromechanical Systems," Proceedings of the SPIE, 3046:24-27.
19. Robbins, W. P., D. L. Polla, and D. E. Glumac. 1991. "High-displacement piezoelectric actuator utilizing a mender-line geometry-Part I: Experimental Characterization," IEEE Transactions on Ultrasonics, Ferroelectrics, and Frequency Control, 38(5):454-459.
20. Catalog of Burleigh Instrument, Inc. 1975. "Micro Positioning System," Fisher, NY.
21. Kurosawa, M., H. Yamada, S. Ueha. 1989. "Hybrid Transducer Type Ultrasonic Motor Using Flexural Vibrator," J. J. Appl. Phys., 30:209-211.
22. Miesner, J. E. and J. P. Teter. 1994. "Piezoelectric/Magnetostrictive resonant inchworm motor," Proceedings of the SPIE, 2190:520-527.
23. Dong, S., L. Li, Z. Gui, T. Zhou, and X. W. Zhang. 1995. "A New Type of Linear Piezoelectric Stepper Motor," IEEE Transactions on Components, Packaging and Manufacturing Technology, Part A, 18(2):257-260.
24. Zhu, J., D. Wang, C. J. Kim, and G. P. Carman. 1996. "Development of Mesoscale Actuator Device," Proceedings of ASME Aerospace Division, IMECE'96:649-654.
25. Chen, Q. D. J. Yao, C. J. Kim, and G. P. Carman. 1998. "Development of mesoscale actuator device with microinterlocking mechanism," Journal of Intelligent Material Systems and Structure, 9: 449-457.
26. Chen, Q., D. J. Yao, C. J. Kim, and G. P. Carman. 1998. "Influence of Fabrication and Crystal Orientation on the Strength of Silicon Microridges," Proceedings of MEMS, ASME Int. Mech. Eng. Congress and Exposition, DSC-66:413-420.
27. Chen, Q., L. H. Chu, D. J. Yao, G. P. Carman, and C. J. Kim. 1999. "Investigation of Large Force Mesoscale Actuator Device and Strength of Its Microridges," submitted to ASME conference.
28. Park, J., Mitrovich, M., Carman, G. P., and H. T. Hahn. 2000. "Design and Testing of a Mesoscale Actuator Device (MAD)," Proceedings of SPIE, 3985.
29. Manual of ANSYS, "Direct coupled-field analysis," Chapter 3.
30. Park, J. 1999. "Design and testing of Mesoscale Actuator Device," Prospectus of thesis dissertation, University of California, Los Angeles: 41.
31. Baumel, A and T Seegur. 1990. "Materials Data for Cyclic Loading," Elsevier Science Publishing Company, Inc., Supplement 1:A.154-A.156.
32. Marin, J. 1962. "Mechanical behavior of engineering materials" Prentice-Hall, Englewood Cliff, N. J.:224.